Lee et al. *NPG Asia Materials* (2022) 14:31
https://doi.org/10.1038/s41427-022-00380-w

NPG Asia Materials

ARTICLE Open Access

# Possible permanent Dirac- to Weyl-semimetal phase transition by ion implantation

Won Jun Lee[1], Yusuff Adeyemi Salawu[2], Heon-Jung Kim[2], Chan Wook Jang[1], Sung Kim[1], Thomas Ratcliff[3], Robert G. Elliman[3], Zengji Yue[4], Xiaolin Wang[4], Sang-Eon Lee[5], Myung-Hwa Jung[5], Jong-Soo Rhyee[1] and Suk-Ho Choi[1]

## Abstract

Three-dimensional (3D) topological semimetals (TSMs) are a new class of Dirac materials that can be viewed as 3D graphene and are referred to as Dirac semimetals (DSMs) or Weyl semimetals (WSMs) depending on whether time reversal symmetry and/or inversion symmetry are protected, respectively. Despite some interesting results on Dirac- to Weyl-semimetal phase transitions under conditions of low temperature or strong magnetic field (B), all of them are reversible phenomena. Here, we report for the first time a possible permanent transition in a single TSM by ion implantation. A Dirac- to Weyl-semimetal phase transition in a $Bi_{0.96}Sb_{0.04}$ DSM results from inversion-symmetry breaking induced by implantation with nonmagnetic Au ions for implant fluences ($\phi_G$) $\geq 3.2 \times 10^{16}$ Au cm$^{-2}$. This phenomenon is evidenced by the $\phi_G$-dependent behavior of the Raman spectra and quantum-oscillation parameters extracted from magnetoresistance (MR) measurements, which show abrupt changes at $\phi_G \geq 3.2 \times 10^{16}$ Au cm$^{-2}$. The verification of the transition is further supported by observations of negative MR in the longitudinal B // electric field orientation, indicating the existence of a chiral anomaly in Weyl fermions induced by implantation with nonmagnetic Au ions. In contrast, implantation with magnetic Mn ions exhibits no such particular behavior. Our findings demonstrate the first realization of a possible permanent DSM-to-WSM phase transition in a single material by the simple approach of implantation using nonmagnetic elements.

## Introduction

Studies on topological semimetals (TSMs), highly attractive as a novel class of topological matter, are at the frontiers of materials science and technology, with many theoretical and experimental breakthroughs being made on several TSM phases, such as Dirac semimetals (DSMs), Weyl semimetals (WSMs), nodal-line semimetals, and triple-point semimetals[1,2]. A broad range of novel transport properties, such as extremely large magnetoresistances, chiral anomalies, and the intrinsic anomalous Hall effect, have been experimentally demonstrated and attributed to relativistic fermions that represent low-energy excitations around the Dirac/Weyl nodal points or nodal line. DSM fermions are the three-dimensional (3D) counterpart of the two-dimensional (2D) Dirac fermions in graphene[3]. Unlike the Dirac cone in graphene, the dispersion surfaces in DSMs have linear energy-momentum relations along all three directions[4,5]. A crystal needs both time reversal symmetry and inversion symmetry to protect the degeneracy of a Dirac node from splitting into two Weyl nodes[6,7]. At the critical point during the transition from a topological insulator to a normal insulator, the conduction and valence band contact points are 3D Dirac or Weyl points, depending on whether inversion symmetry exists or not, respectively. Berry curvature, a quantity that can be used to characterize the topological entanglement between the

Correspondence: Suk-Ho Choi (sukho@khu.ac.kr)
[1]Department of Applied Physics, Institute of Natural Sciences, and Integrated Education Institute for Frontier Science and Technology (BK21 Four), Kyung Hee University, Yongin 17104, Republic of Korea
[2]Department of Physics, College of Natural Science, Daegu University, Gyeongbuk 712-714, Republic of Korea
Full list of author information is available at the end of the article
These authors contributed equally: Won Jun Lee, Yusuff Adeyemi Salawu.

conduction and valence bands, becomes singular at Weyl points that act as monopoles in momentum space with a fixed chirality[8–10].

The crystal structure of pure Bi, pure Sb, and their crystalline alloys ($Bi_{1-x}Sb_x$) that can be formed over a wide range of x is rhombohedral, and all have $R\bar{3}m$ symmetry with two atoms in each unit cell[11]. In Bi, pockets of electrons are located at the L points of the Brillouin zone (BZ), while those of holes are located at the T points. The valence band (VB) and conduction band (CB) at L originate from antisymmetric ($L_a$) and symmetric ($L_s$) p-type orbitals, respectively[12]. In Sb, pockets of electrons are also located at the L points of the BZ, while those of holes are located at the H points. The substitution of Sb atoms for Bi atoms in the Bi lattice has a significant effect on the band structure of Bi, including the overlap between the L and T bands, the magnitude of the direct band gap $E_g$, and the maximum energy of the H bands. For Sb concentrations ($x$) between $0 \le x < 0.04$, the overlap and band gap decrease. At $x = 0.04$, the CB and VB edges exchange their symmetries at the $L$ points, thereby closing the L-point energy gap between $L_a$ and $L_s$, resulting in the formation of a DSM[13,14].

For materials research, ion implantation offers two main advantages: (1) it is a room temperature (RT) process, enabling doping and annealing processes to be studied independently; and (2) it enables selective doping of devices and structures with different species. Here, we compare the magnetoresistance (MR) response of $Bi_{0.96}Sb_{0.04}$ DSMs ion-implanted with Au and Mn ions and demonstrate a possible permanent Dirac- to Weyl-semimetal phase transition in samples implanted with Au. No such behavior is observed in samples implanted with Mn, suggesting that only nonmagnetic elements are effective for the transition.

## Materials and methods

$Bi_{0.96}Sb_{0.04}$ bulk single crystals with 99.99% purity were grown in a high-temperature furnace using a method previously reported[12]. Stoichiometric mixtures of high-purity Bi and Sb elements were sealed in a vacuum quartz tube to avoid oxidation. The mixtures were heated to 650 °C and cooled to 270 °C over a period of five days. Then, they were annealed for seven days at 270 °C. X-ray diffraction measurements demonstrated that the samples were single phase and had a rhombohedral crystal structure. $Bi_{0.96}Sb_{0.04}$ crystals cleaved along the (001) plane from the bulk crystals were implanted with 1 MeV $Au^+$ ions to nominal fluences of $(0.8, 3.2, 8.0, 10.4, \text{and } 12.8) \times 10^{16}$ Au cm$^{-2}$ or with 300 keV $Mn^+$ ions to nominal fluences of $(4.0 \text{ and } 8.0) \times 10^{16}$ Mn cm$^{-2}$ at RT. The peak Au or Mn concentrations for these implantations were calculated from dynamic range simulations using the TriDyn code[15] to be in the range of 1.7–5.6 at% ($0.48–1.6 \times 10^{21}$ Au cm$^{-3}$) or 5.8–10.3 at% ($1.6–2.9 \times 10^{21}$ Mn cm$^{-3}$), respectively. The implanted crystals were subsequently annealed at 230 °C for 1 h in a furnace under Ar flow to remove the implantation-induced damage.

Raman spectroscopy was used to characterize the optical properties of the $Bi_{0.96}Sb_{0.04}$ crystals cleaved along the (001) plane from the bulk crystals in a confocal microscope system (HEDA, NOST) with an excitation wavelength of 532 nm at RT. The laser was coupled to a ×100 objective lens (numerical aperture = 0.90) and focused to a submicrometer spot on the sample surface. The Raman signal collected with the same objective was dispersed through a monochromator with a diffraction grating of 2400 grooves/mm and detected by a charge-coupled device (Andor Technology). The Raman spectra were measured from the shiny silver-colored surface of the crystals for various $\phi_G$ in the frequency range from 50 to 180 cm$^{-1}$. The penetration depth of the X-rays is much deeper than the implantation depth, so a technique of glancing incidence was employed for the XRD analysis. Magnetotransport experiments were carried out on the $Bi_{0.96}Sb_{0.04}$ crystals in a cryogen-free magnet system under B ranging from −9 T to +9 T along the directions parallel and perpendicular (B // trigonal axis for transverse MR (TMR) and B // binary axis for longitudinal MR (LMR), respectively) to the applied current $I$ (// binary axis) using the six-probe method. Homogenous contact configurations were employed to suppress the current jetting effect of the MR, as described in our previous report[16]. All electrical contacts were prepared at RT with silver paste. The TMR and Hall resistance were simultaneously measured when B was perpendicular to $I$. The electrical resistivity of the crystals under no B field was also measured as a function of temperature from 1.7 to 300 K.

## Results and discussion

$Bi_{0.96}Sb_{0.04}$ crystals cleaved along the (001) plane from bulk crystals with 99.99% purity were implanted with 1 MeV $Au^+$ ions to nominal fluences ($\phi_G$) of (0.8, 3.2, 8.0, 10.4, and 12.8) × $10^{16}$ Au cm$^{-2}$ at RT. The Au range distributions were calculated using the TriDyn code[15], which includes sputtering effects. This showed that the peak Au concentration saturated at ~5.6 at% for ion fluences above ~$6 \times 10^{16}$ Au cm$^{-2}$. (Supplementary Fig. S1). X-ray diffraction analysis of the implanted crystals was performed for various $\phi_G$ in the angular range of $2\theta_{min} = 20°$ and $2\theta_{max} = 80°$ (Supplementary Fig. S2). All the samples exhibited sharp (00l) reflections that were well indexed along the $c$-axis, indicating a single-crystalline, $c$-axis-oriented rhombohedral structure of the space group $R\bar{3}m$[11–13]. An additional peak appeared at $2\theta \approx 49.5°$ along with the characteristic peaks of the (00l) plane for all the

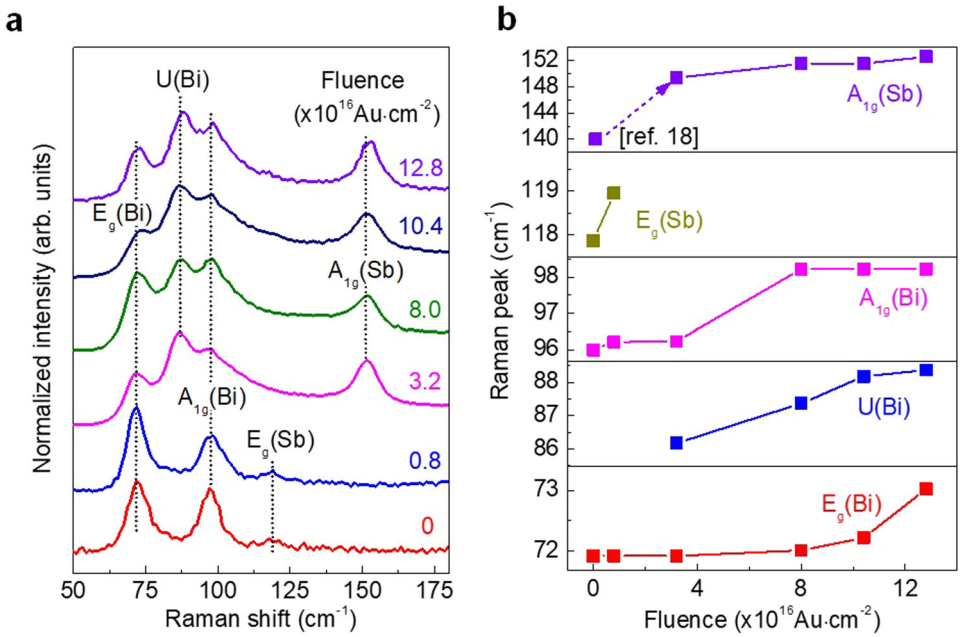


**Fig. 1 Effect of implantation on Raman spectra. a** Raman spectra of $Bi_{0.96}Sb_{0.04}$ for various implant fluences. The $E_g$(Bi)/$A_{1g}$(Bi) and $E_g$(Sb)/$A_{1g}$(Sb) peaks indicate Bi–Bi and Sb-Sb vibration modes, respectively, and the $A_{1g}$ modes are singly degenerate, while the $E_g$ modes are doubly degenerate. The additional U(Bi) peak is an unknown new mode, different from the $E_g$ and $A_{1g}$ modes expected from group theory for the rhombohedral structure. **b** Shifts of the Raman peaks as functions of implant fluence.

samples and was identified as the (202) peak, originating from the misaligned plane of $Bi_{0.96}Sb_{0.04}$[17]. The XRD patterns did not show any particular dependence on $\phi_G$, even though a technique of glancing incidence was employed considering that the penetration depth of the X-rays was much deeper than the implanted layer. This is possible because the XRD patterns do not reflect the (111) plane (L point of the BZ) directly related to the inversion symmetry of $Bi_{0.96}Sb_{0.04}$ DSMs[12,18].

Figure 1a shows the $\phi_G$-dependent Raman spectrum of $Bi_{0.96}Sb_{0.04}$. At $\phi_G = 0$ (without implantation), two peaks are clearly observed at 72.3 and 97.5 $cm^{-1}$, referred to as $E_g$(Bi) and $A_{1g}$(Bi), respectively, while one other peak is weakly visible at 119 $cm^{-1}$, referred to as $E_g$(Sb)[17,19,20]. It is well known that the $Bi_{1-x}Sb_x$ system commonly exhibits four major Raman peaks, two of which are observed at ~72–75 and ~97–100 $cm^{-1}$ and correspond to the Bi–Bi vibrations of the $E_g$(Bi) and $A_{1g}$(Bi) modes, respectively, typical of single crystals with rhombohedral $R\bar{3}m$ symmetry[17,21], and the other two peaks are observed at ~118–120 and ~138–141 $cm^{-1}$ and correspond to the Sb–Sb vibrations of the $E_g$(Sb) and $A_{1g}$(Sb) modes[17,19,20]. The $A_{1g}$ mode is singly degenerate, while the $E_g$ mode is doubly degenerate. In our $Bi_{0.96}Sb_{0.04}$ system, the $A_{1g}$(Sb) mode is absent before implantation, possibly due to local deviation from the stoichiometric condition, as the $A_{1g}$(Sb) mode is very sensitive to the atomic compositions of the crystal[19,20].

Figure 1a also shows little change from the three Raman peaks of the pristine (unimplanted) $Bi_{0.96}Sb_{0.04}$ crystal for implant fluences up to $\phi_G = 0.8 \times 10^{16}$ Au $cm^{-2}$, but a drastic change is observed for fluences above $\phi_G = 3.2 \times 10^{16}$ Au $cm^{-2}$. In particular, a new peak appears at 85.7 $cm^{-1}$ between the $E_g$(Bi) and $A_{1g}$(Bi) modes, named U(Bi). It is not clear whether the U(Bi) mode is split from the $E_g$(Bi) mode or the $A_{1g}$(Bi) mode. Moreover, the $A_{1g}$(Sb) peak, absent in the pristine $Bi_{0.96}Sb_{0.04}$ crystal, appears at 149.7 $cm^{-1}$, which is a higher wavenumber than that conventionally reported (~138–141 $cm^{-1}$), indicating that the $A_{1g}$(Sb) peak is blueshifted by implantation to $\phi_G = 3.2 \times 10^{16}$ Au $cm^{-2}$. The overall shape of the Raman spectrum for $\phi_G = 3.2 \times 10^{16}$ Au $cm^{-2}$ is almost unchanged as the fluence is increased to $12.8 \times 10^{16}$ Au $cm^{-2}$ except for a gradual increase in the peak wavenumber. Some of the Raman spectra were resolved into the $E_g$(Bi), $A_{1g}$(Bi), and U(Bi) bands to find their peak positions more accurately based on the fitting program (Supplementary Fig. S3). Figure 1b summarizes the shifts of the Raman modes as functions of $\phi_G$. As $\phi_G$ increases from 0 to $12.8 \times 10^{16}$ Au $cm^{-2}$, the four $E_g$(Bi), U(Bi), $A_{1g}$(Bi), and $A_{1g}$(Sb) modes tend to be gradually blueshifted.

All the Raman peaks of $MoTe_2$ are known to stem from two kinds of vibrations: (1) those along the zigzag Mo atomic chain (z-modes) and (2) those in the mirror plane (m-modes) perpendicular to the zigzag chain[22]. Some

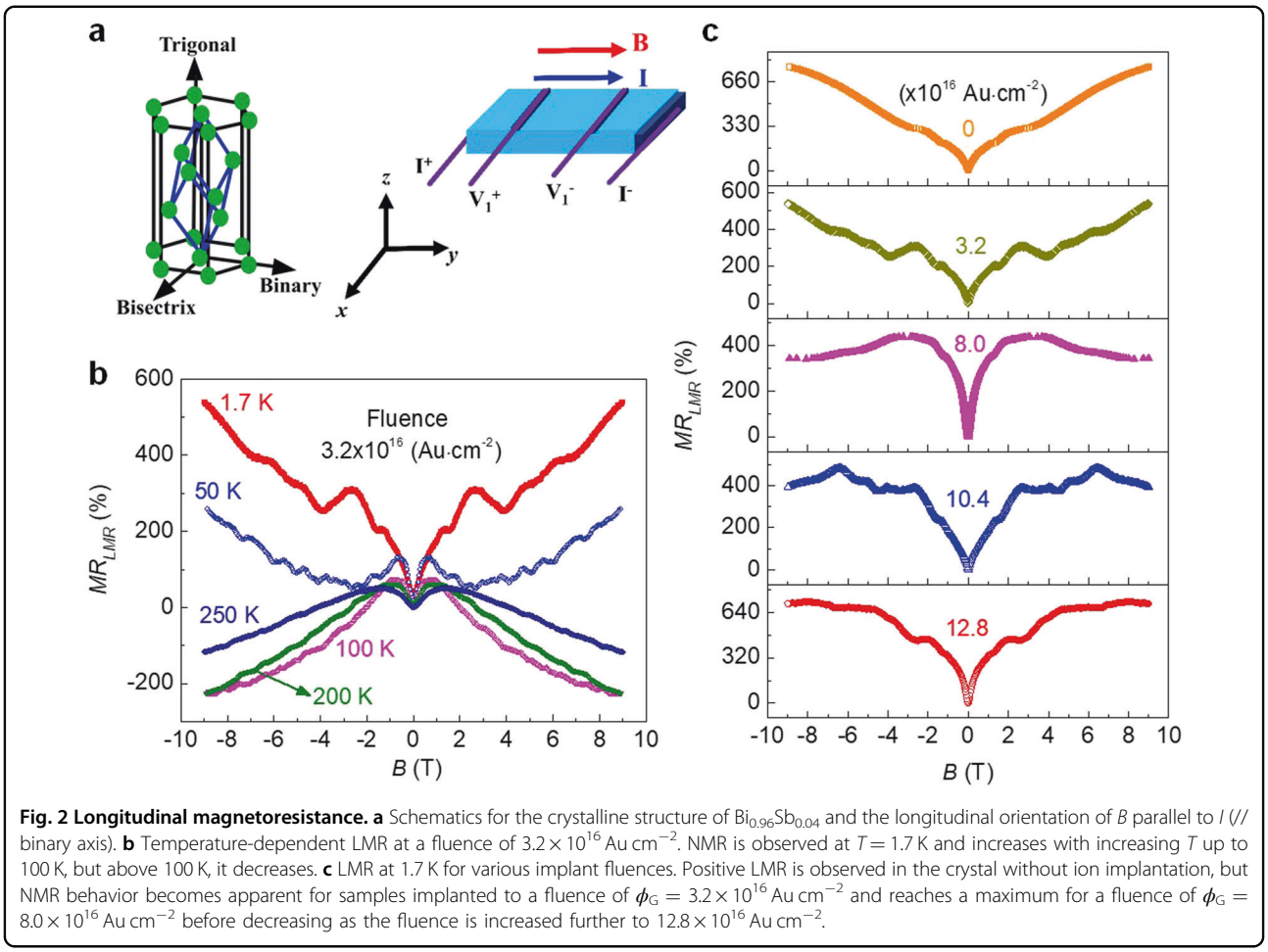


**Fig. 2 Longitudinal magnetoresistance. a** Schematics for the crystalline structure of $Bi_{0.96}Sb_{0.04}$ and the longitudinal orientation of *B* parallel to *I* (// binary axis). **b** Temperature-dependent LMR at a fluence of $3.2 \times 10^{16}$ Au cm$^{-2}$. NMR is observed at $T = 1.7$ K and increases with increasing *T* up to 100 K, but above 100 K, it decreases. **c** LMR at 1.7 K for various implant fluences. Positive LMR is observed in the crystal without ion implantation, but NMR behavior becomes apparent for samples implanted to a fluence of $\phi_G = 3.2 \times 10^{16}$ Au cm$^{-2}$ and reaches a maximum for a fluence of $\phi_G = 8.0 \times 10^{16}$ Au cm$^{-2}$ before decreasing as the fluence is increased further to $12.8 \times 10^{16}$ Au cm$^{-2}$.

Raman inactive modes in the centrosymmetric monoclinic phase appear in the cooling-driven transition to the orthorhombic phase[22,23], resulting from inversion-symmetry breaking, which is evidence for the formation of a type II WSM. On the other hand, the appearance of a Raman doublet at a higher composition of W in monoclinic $Mo_{1-x}W_xTe_2$ alloys was attributed to the breakdown of inversion symmetry, which originates from the random substitution of Mo atoms with W atoms[24]. These results suggest that whether inversion symmetry in a crystalline structure is broken can be determined by analyzing the Raman scattering behaviors.

Very recently, inversion symmetry breaking was also demonstrated by first-principle calculations and Raman scattering of the $CdTiO_3$ ilmenite phase belonging to the rhombohedral $R\bar{3}m$ group[21]. Additional Raman peaks, different from the $E_g$ and $A_g$ modes expected from group theory for the ilmenite rhombohedral structure, appeared in both low-temperature and high-pressure spectra, with the Raman wavenumbers being blueshifted at higher pressures. These results were very similar to the $\phi_G$-dependent Raman behavior observed here for the $Bi_{0.96}Sb_{0.04}$ crystal and were successfully accounted for by assuming the local loss of inversion symmetry operation, which reduces the overall space group from $R\bar{3}$ to R3. Such arguments can be extended to the $Bi_{0.96}Sb_{0.04}$ crystal with the same rhombohedral $R\bar{3}$ symmetry, suggesting that inversion symmetry breaking in the crystal occurred for implant fluences $\phi_G \geq 3.2 \times 10^{16}$ Au.cm$^{-2}$, resulting in the transition of the DSM $Bi_{0.96}Sb_{0.04}$ to a Weyl semimetal.

MR measurements under parallel (B // E) (i.e., B parallel to the binary axis for LMR and perpendicular (B ⊥ E) (i.e., B parallel to the trigonal axis for TMR) orientations in TSMs always show different behavior, as orbital quantum interference effects are sensitive to the field orientation [25–27]. Parallel (B // E) measurements for the present samples are shown in Fig. 2a, with perpendicular (B ⊥ E) measurements included in Supplementary Fig. S4a. It has also been observed that the LMR in some TSMs shows a sharp increase as the B field is initially increased from zero, before decreasing at intermediate fields and then further increasing at higher fields. This phenomenon is referred to as negative LMR (NMR)[27–30]. Significantly,

NMR is only observed in the B // E orientation and not in the B ⊥ E orientation[30,31], consistent with current observations (Supplementary Fig. S4b). Figure 2b shows the T-dependent LMR of the $Bi_{0.96}Sb_{0.04}$ crystal at $\phi_G = 3.2 \times 10^{16}$ Au cm$^{-2}$, measured from −9 to +9 T. The amplitude of the NMR is observed at $T = 1.7$ K and increases with increasing $T$ up to 100 K, but above 100 K, it decreases. Similar temperature-dependent behavior has been reported in WSMs by several groups. In $Cd_3As_2$ nanowires[28], the NMR increased as $T$ increased from 1.5 to 60 K but decreased as it increased further from 80 to 300 K. The NMR found in $Cd_3As_2$ nanoplates[32] and NbP[31] increased monotonically with increasing temperature up to 150 and 300 K, respectively. In contrast, the NMR in TaAs decreased monotonically with increasing $T$[27,29].

Figure 2c shows the variation in the LMR at 1.7 K for various implant fluences. Positive LMR is observed in the crystal with no ion implantation, but NMR behavior becomes apparent for samples implanted to a fluence of $\phi_G = 3.2 \times 10^{16}$ Au cm$^{-2}$ and reaches a maximum for a fluence of $\phi_G = 8.0 \times 10^{16}$ Au cm$^{-2}$ before decreasing as the fluence is increased further to $12.8 \times 10^{16}$ Au cm$^{-2}$. In contrast, only positive MR is observed from Mn-implanted $Bi_{0.96}Sb_{0.04}$ crystals, irrespective of the relative orientation of the B and E fields and $\phi_G$ (Supplementary Fig. S5). Implantation with Mn ions is expected to break both time reversal and inversion symmetries because Mn is a magnetic element, implying that no phase transition from DSM to WSM occurred and that the crystal was potentially changed into a trivial metallic state by Mn implantation. If no magnetic exchange interaction exists, conventional metals should exhibit positive MR[33,34], and the appearance of a negative MR in normal metals is limited to special cases[35,36]. An important aspect of NMR is that it confirms the existence of a chiral anomaly in Weyl fermions, as shown in $Cd_3As_2$[28,32], $Bi_{0.97}Sb_{0.03}$[37], TaAs[27,29], $ZrTe_5$[38], $Na_3Bi$[39], and NaP[31]. These results are similar to the $\phi_B$-dependent Raman behavior shown in Fig. 1 and further suggest that the implantation-induced Dirac- to Weyl-semimetal phase transition is enabled by a nonmagnetic element (Au) rather than a magnetic element (Mn).

Figure 3a shows Shubnikov–de Haas (SdH) oscillations as a function of $1/B$ as extracted from the $\phi_G$-dependent LMR data in Fig. 2c after background subtraction. Fast Fourier transform (FFT) analysis for $\phi_G = 0$, 3.2, and $12.8 \times 10^{16}$ Au cm$^{-2}$, shown in Fig. 3b, reveals the primary and secondary frequencies ($F_\alpha$ and $F_\beta$) of the SdH oscillations, which are plotted in Fig. 3c as a function of $\phi_G$. The validity of the fitting was checked by separately plotting the two components of the SdH oscillations and summing them (Supplementary Fig. S6), resulting in almost coincidence of the summed oscillatory profiles with the original experimental data. The variation in $F_\alpha$ is almost negligible, but $F_\beta$ increases abruptly at a fluence of $\phi_G = 3.2 \times 10^{16}$ Au cm$^{-2}$.

The SdH quantum oscillations are usually described by the Lifshitz–Kosevich (LK) formula[8,40–43], and the corresponding parameters for both the $\alpha$ and $\beta$ Fermi pockets can be obtained by fitting the FFT amplitude data based on the LK formula, as detailed previously[8,9,40–43]. The SdH oscillation of resistance in a metal arises from the Landau quantization of electronic states under an applied B-field. Based on the Lifshitz–Onsager quantization rule described by $A_F \frac{\hbar}{eB} = 2\pi\left(n + \frac{1}{2} - \frac{\phi_B}{2\pi}\right) = 2\pi(n + \phi)$[8,9,43,44], where $\hbar$ is the reduced Planck's constant and $e$ is the elementary charge, the phase shift $\phi$ (= 1/2− $\phi_B$/2π) in the Landau fan diagram gives the Berry phase $\phi_B$. Almost all the extracted parameters, such as the Dingle temperature ($T_D$), quantum scattering time ($\tau_Q$), carrier density ($n_{3D}$), quantum mobility ($\mu_Q$), cross-sectional area of the Fermi pockets ($A_F$), cyclotron mass ($m^*$), Fermi velocity ($v_F$), Fermi wave vector ($k_F$), mean free path ($l_Q$), and Fermi level ($E_F$), except $\phi$ for the $\alpha$ Fermi pocket, do not show any particular dependences on $\phi_G$, as shown in Fig. 3d–g (and Supplementary, Fig. S7). For the $\beta$ Fermi pocket, almost all the parameters except $\phi$ show negligible variations at $\phi_G = 0.8 \times 10^{16}$ Au.cm$^{-2}$, but with the increase of $\phi_G$ to $3.2 \times 10^{16}$ Au.cm$^{-2}$, they show abrupt changes (increase or decrease), and by further increasing $\phi_G$ above $3.2 \times 10^{16}$ to $12.8 \times 10^{16}$ Au cm$^{-2}$, only small variations in the parameters are observed, consistent with the $\phi_G$-dependent Raman and LMR behaviors, as shown in Figs. 1 and 2, respectively. In particular, the reliability of the estimated $m^*$ was cross-checked by considering the temperature dependence of the SdH oscillations at several implant fluences[45]. The fit of the SdH oscillation amplitudes at various temperatures to the thermal damping factor yielded $m^*$ values (Supplementary Fig. S8) nearly the same as those estimated by direct fitting (Supplementary Fig. S7b).

WSMs possess nontrivial topological surface states that form unique Fermi arcs[1,2,46] and unusual Fermi surfaces consisting of unclosed curves that start and end at Weyl points split from a Dirac point. This explains why $A_F$ should increase in the Dirac- to Weyl-semimetal phase transition at $\phi_G \geq 3.2 \times 10^{16}$ Au cm$^{-2}$, as shown for the $\beta$ Fermi pocket in Fig. 3d. In contrast, no meaningful variation in $A_F$ is visible for the $\alpha$ Fermi pocket, indicating that the phase transition occurs only in the $\beta$ Fermi pocket. The $A_F$ of the $\beta$ Fermi pocket (~0.09 nm$^{-2}$ in Fig. 3d) is extremely small, indicating linear band dispersion, as previously reported[47,48]. Combining this fact with the inversion symmetry breaking further explains why $Bi_{0.96}Sb_{0.04}$ implanted to $\phi_G \geq 3.2 \times 10^{16}$ Au cm$^{-2}$ should show NMR. It is well known that a π $\phi_B$ is expected for

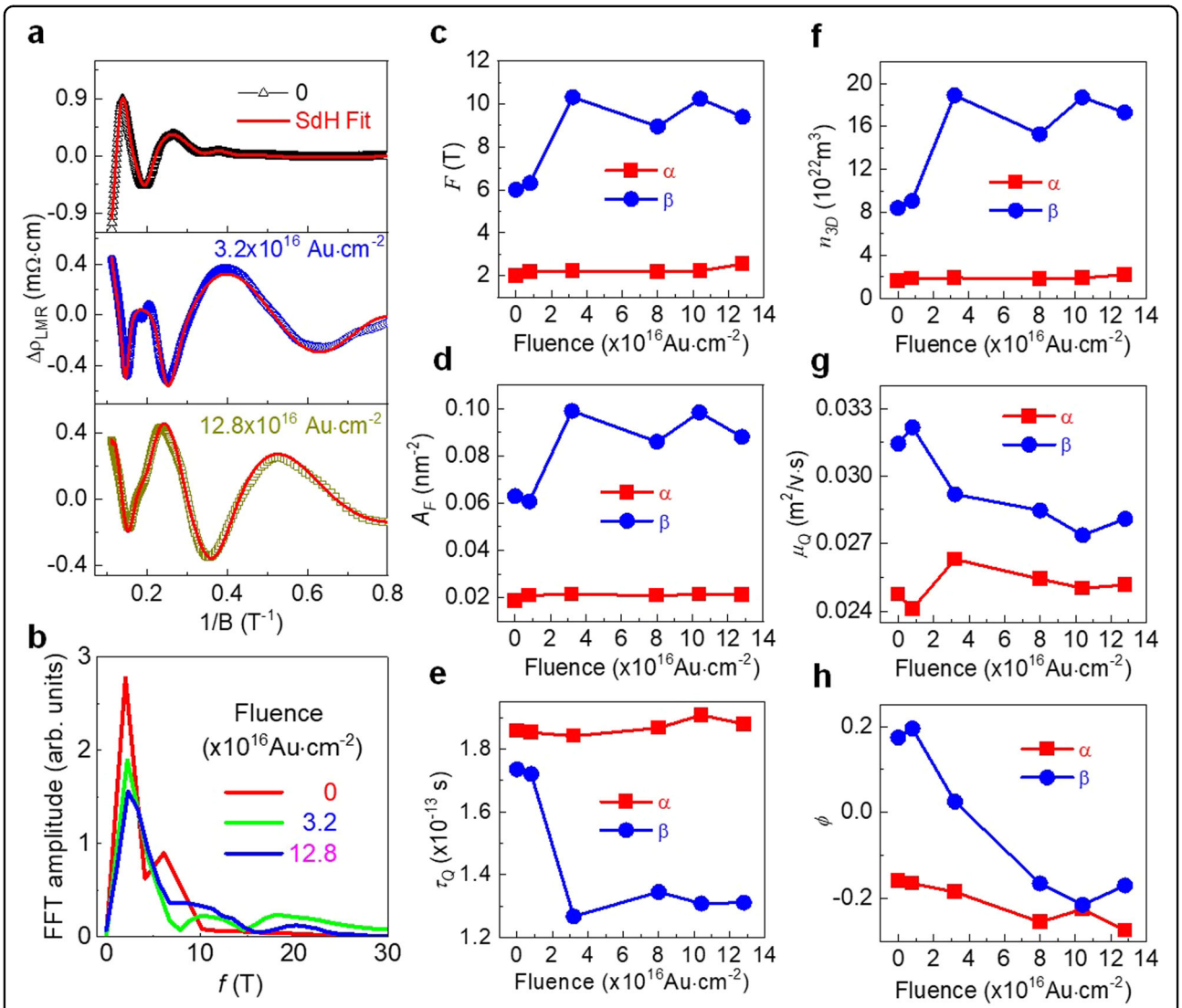


**Fig. 3 Quantum oscillations and extracted parameters. a** Resistivities as functions of 1/B and **b** fast Fourier transform (FFT) spectra for implant fluences of (0, 3.2, and 12.8) x $10^{16}$ Au.cm$^{-2}$. The SdH oscillations in **a** were extracted from the LMR data in Fig. 2c after background subtraction. **c** Frequency, **d** cross-sectional area ($A_F$), **e** quantum scattering time ($\tau_Q$), **f** carrier density ($n_{3D}$), **g** quantum mobility ($\mu_Q$), and **h** phase shift ($\phi$) of the $\alpha$ and $\beta$ Fermi pockets as functions of implant fluence.

DSMs such as the pristine $Bi_{0.96}Sb_{0.04}$ crystal because their electronic band is topologically nontrivial[8,9,40,43]. As shown in Fig. 3h, the $\phi$ values for the $\alpha$ and $\beta$ Fermi pockets show somewhat different dependences on $\phi_G$ compared to the other parameters of the quantum oscillations, as shown above. They show gradually decreasing behavior with increasing fluence from 0 to $12.8 \times 10^{16}$ Au cm$^{-2}$, with the decreasing rate being much smaller for the $\alpha$ pocket. The $\phi$ values for the $\beta$ Fermi pocket are within ±~0.2. This near-zero $\phi$, with zero being the widely accepted value for 3D DSMs/WSMs[8,49,50], possibly indicates a nontrivial π $\phi_B$. An increase or decrease in the other parameters for the $\beta$ Fermi pocket at $\phi_G \geq 3.2 \times 10^{16}$ Au cm$^{-2}$ can be understood by simple physical considerations and the following related equations[40–43]: $F = (\hbar/2\pi e)A_F$, $T_D = \hbar/2\pi k_B \tau_Q$, $k_F = \sqrt{2eF/\hbar}$, $E_F = (\hbar k_F)^2/m^*$, $l_Q = v_F \cdot \tau_Q$, $v_F = \hbar k_F/m^*$, and $\mu_Q = e\tau_Q/m^*$. These results suggest that the $\alpha$ Fermi pocket remains a Dirac semimetal phase even after implantation.

Figure 4a shows the $\phi_G$-dependent resistivity as a function of T under no B field. All the samples show an increase in resistivity with temperature, irrespective of $\phi_G$, typical of TSMs. Figure 4b–d shows $\phi_G$-dependent resistivity, carrier density, and mobility for the $F_\beta$ and $F_\alpha$ Fermi pockets obtained by Hall-effect measurements.

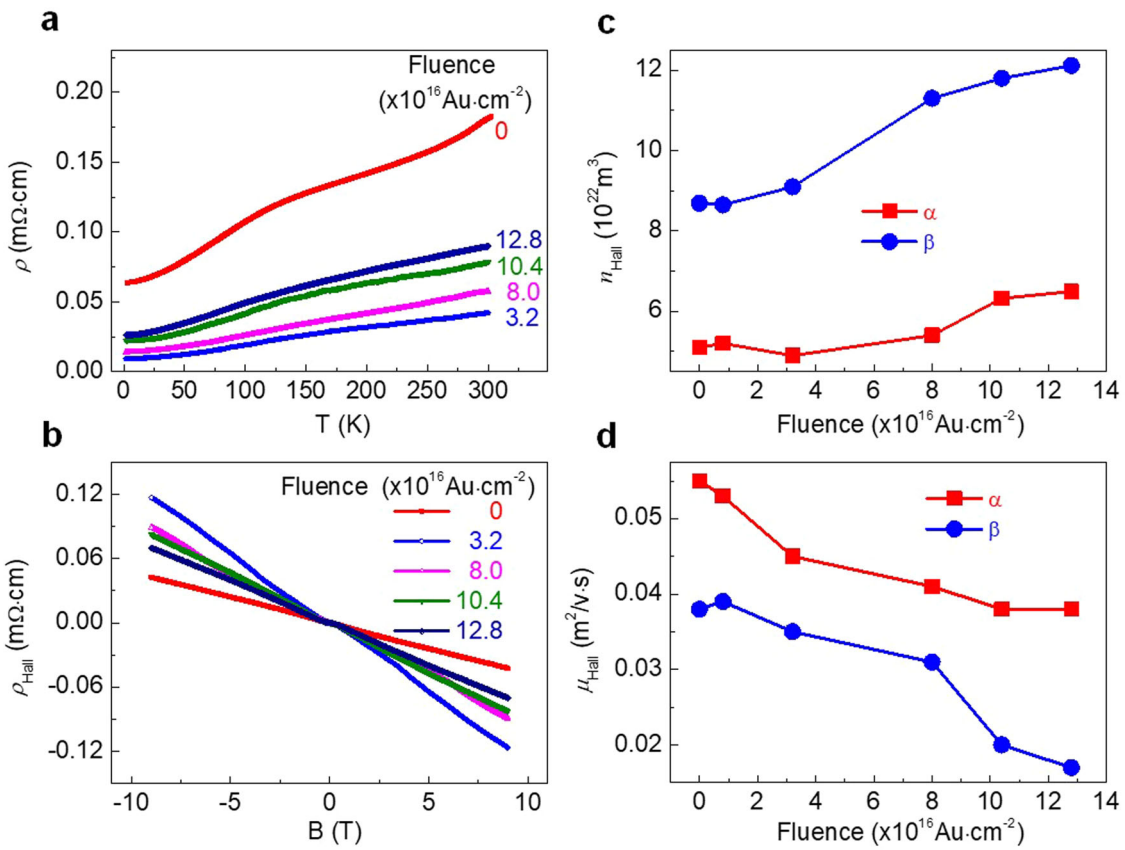


**Fig. 4 Electrical and Hall-effect properties. a** Electrical resistivities as functions of temperature under no B field for various implant fluences. **b** Hall resistivities as functions of B for various implant fluences. **c** Hall carrier densities and **d** mobilities as functions of implant fluence for the *α* and *β* Fermi pockets.

Abrupt changes at $\phi_G = 3.2 \times 10^{16}$ Au cm$^{-2}$, as shown in the $\phi_G$-dependent behaviors of the Raman scattering and quantum oscillations, were not observed in the Hall mobility or carrier density, but both show $\phi_G$-dependent behavior for both Fermi pockets, consistent with what is expected from the fundamental characteristics of materials with larger impurity concentrations.

## Conclusion

Here, we demonstrated a possible permanent Dirac- to Weyl-semimetal phase transition in a single DSM resulting from inversion-symmetry breaking induced by implantation with nonmagnetic Au ions. This phenomenon is evidenced by Raman analysis and the quantum-oscillation parameters extracted from the LMR, which show abrupt changes at the critical fluence, and the negative LMR, indicating the existence of a chiral anomaly in Weyl fermions. The approach of implantation using nonmagnetic elements for phase transitions may be a suitable method for simple modifications of TSMs in the vertical direction as well as in the lateral direction and useful for diverse science studies and device applications.

**Acknowledgements**

This work was supported by a National Research Foundation of Korea (NRF) grant funded by the Korean government (MSIT) (No. 2020R1A2C2004376). Z.Y. and X.-L.W. acknowledge partial support from the ARC Centre of Excellence in Future Low-Energy Electronics Technologies (No. CE170100039), funded by the Australian Government. The authors also acknowledge access to the Australian Facility for Advanced ion-implantation Research (AFAiiR), a facility funded by the Australian Government's National Collaborative Research Infrastructure Strategy (NCRIS).

**Author details**

[1]Department of Applied Physics, Institute of Natural Sciences, and Integrated Education Institute for Frontier Science and Technology (BK21 Four), Kyung Hee University, Yongin 17104, Republic of Korea. [2]Department of Physics, College of Natural Science, Daegu University, Gyeongbuk 712-714, Republic of Korea. [3]Department of Electronic Materials Engineering, Research School of Physics and Engineering, The Australian National University, Canberra, ACT 0200, Australia. [4]Institute for Superconducting and Electronic Materials, Australian Institute for Innovative Materials, University of Wollongong, North Wollongong, NSW 2500, Australia. [5]Department of Physics, Sogang University, Seoul, Republic of Korea

**Author contributions**

W.J.L. carried out the Raman and XRD measurements. Y.A.S. obtained the MR and Hall-effect data. C.W.J. and S.K. analyzed the Raman and XRD data. H.-J.K. and J.-S.R. interpreted the MR and quantum oscillation data. T.R. and R.G.E. performed the SRIM simulation and ion implantation. Z.Y. and X.-L.W. prepared the single crystals. S.L. and M.-H.J. performed the annealing experiments. S.-H.C.

initiated and supervised the work and wrote the paper. All authors discussed the results and commented on the manuscript.

### Competing interests
The authors declare no competing interests.

### Publisher's note
Springer Nature remains neutral with regard to jurisdictional claims in published maps and institutional affiliations.

**Supplementary information** The online version contains supplementary material available at https://doi.org/10.1038/s41427-022-00380-w.

Received: 1 August 2021 Revised: 21 February 2022 Accepted: 10 March 2022.
Published online: 8 April 2022

### References
1. Armitage, N. P., Mele, E. J. & Vishwanath, A. Weyl and Dirac semimetals in three-dimensional solids. *Rev. Mod. Phys.* **90**, 015001 (2018).
2. Hu, J., Xu, S.-Y., Ni, N. & Mao, Z. Transport of topological semimetals. *Ann. Rev. Mater. Res.* **49**, 207–252 (2019).
3. Kane, C. L. & Mele, E. J. Quantum spin hall effect in graphene. *Phys. Rev. Lett.* **95**, 226801 (2005).
4. Young, S. M. et al. Dirac semimetal in three dimensions. *Phys. Rev. Lett.* **108**, 140405 (2012).
5. Wan, X., Turner, A. M., Vishwanath, A. & Savrasov, S. Y. Topological semimetal and fermi-arc surface states in the electronic structure of pyrochlore iridates. *Phys. Rev. B* **83**, 205101 (2011).
6. Wang, Z. et al. Dirac semimetal and topological phase transitions in $A_3Bi$ ($A$ = Na, K, Rb). *Phys. Rev. B* **85**, 195320 (2012).
7. Wang, Z., Weng, H., Wu, Q., Dai, X. & Fang, Z. Three dimensional Dirac semimetal and quantum transport in $Cd_3As_2$. *Phys. Rev. B* **88**, 125427 (2013).
8. Wang, C. M., Lu, H.-Z. & Shen, S.-Q. Anomalous phase shift of quantum oscillations in 3D topological semimetals. *Phys. Rev. Lett.* **117**, 077201 (2016).
9. Cao, J. et al. Landau level splitting in $Cd_3As_2$ under high magnetic fields. *Nat. Commun.* **6**, 7779 (2015).
10. Alexandradinata, A., Wang, C., Duan, W. & Glazman, L. Revealing the topology of Fermi-surface wave functions from magnetic quantum oscillations. *Phys. Rev. X* **8**, 011027 (2018).
11. Tang, S. & Dresselhaus, M. S. Electronic properties of nano-structured bismuth-antimony materials. *J. Mater. Chem. C* **2**, 4710–4726 (2014).
12. Hsieh, D. et al. A topological Dirac insulator in a quantum spin Hall phase. *Nature* **452**, 970–974 (2008).
13. Lenoir, B., Cassart, M., Michenaud, J.-P., Scherrer, H. & Scherrer, S. Transport properties of Bi-rich Bi-Sb alloys. *J. Phys. Chem. Solids* **57**, 89–99 (1996).
14. Rogacheva, E. I., Drozdova, A. A., Nashchekina, O. N., Dresselhaus, M. S. & Dresselhaus, G. Transition into a gapless state and concentration anomalies in the properties of $Bi_{1-x}Sb_x$ solid solutions. *Appl. Phys. Lett.* **94**, 202111 (2009).
15. Möller, W. TRI3DYN-Collisional computer simulation of the dynamic evolution of 3-dimensional nanostructures under ion irradiation. *Nucl. Instrum. Methods B* **322**, 23–33 (2014).
16. Shin, D. et al. Violation of Ohm's law in a Weyl metal. *Nat. Mater.* **16**, 1096 (2017).
17. Sultana, R., Gurjar, G., Gahtori, B., Patnaik, S. & Awana, V. P. S. Flux free single crystal growth and detailed physical property characterization of $Bi_{1-x}Sb_x$ (x = 0.05, 0.1 and 0.15) topological insulator. *Mater. Res. Express.* **6**, 106102 (2019).
18. Tang, S. & Dresselhaus, M. S. Phase diagrams of $Bi_{1-x}Sb_x$ thin films with different growth orientations. *Phys. Rev. B* **86**, 075436 (2012).
19. Zitter, R. N. & Watson, P. C. Raman and x-ray spectra of single-crystal Bi-Sb alloys. *Phys. Rev. B* **10**, 607–611 (1974).
20. Lannin, J. S. First-order Raman scattering in $Bi_{1-x}Sb_x$ alloys. *Phys. Rev. B* **19**, 2390–2393 (1979).
21. Rodrigues, J. E. et al. First-principles calculations and Raman scattering evidence for local symmetry lowering in rhombohedral ilmenite: temperature- and pressure-dependent studies. *J. Phys. Condens. Matter* **30**, 485401 (2018).
22. Chen, S.-Y., Goldstein, T., Venkataraman, D., Ramasubramaniam, A. & Yan, J. Activation of new Raman modes by inversion symmetry breaking in Type II Weyl semimetal candidate T′-$MoTe_2$. *Nano Lett.* **16**, 5852–5860 (2016).
23. Zhang, K. et al. Raman signatures of inversion symmetry breaking and structural phase transition in type-II Weyl semimetal $MoTe_2$. *Nat. Commun.* **7**, 13552 (2016).
24. Oliver, S. M. et al. The structural phases and vibrational properties of $Mo_{1-x}W_xTe_2$ alloys. *2D Materials* **4**, 045008 (2017).
25. Zhao, B. et al. Weak antilocalization in $Cd_3As_2$ thin films. *Sci. Rep.* **6**, 22377 (2016).
26. Lin, C. J. et al. Parallel field magnetoresistance in topological insulator thin films. *Phys. Rev. B* **88**, 041307(R) (2013).
27. Zhang, C.-L. et al. Signatures of the Adler–Bell–Jackiw chiral anomaly in a Weyl fermion semimetal. *Nat. Commun.* **7**, 10735 (2016).
28. Li, C. Z. et al. Giant negative magnetoresistance induced by the chiral anomaly in individual $Cd_3As_2$ nanowires. *Nat. Commun.* **6**, 10137 (2015).
29. Huang, X. et al. Observation of the chiral-anomaly-induced negative magnetoresistance in 3D Weyl semimetal TaAs. *Phys. Rev. X* **5**, 031023 (2015).
30. Arnold, F. et al. Negative magnetoresistance without well-defined chirality in the Weyl semimetal TaP. *Nat. Commun.* **7**, 11615 (2016).
31. Niemann, A. C. et al. Chiral magnetoresistance in the Weyl semimetal NbP. *Sci. Rep.* **7**, 43394 (2017).
32. Zhang, C. et al. Room-temperature chiral charge pumping in Dirac semimetals. *Nat. Commun.* **8**, 13741 (2017).
33. Ziman, J. M. in *Handbook of Electrons and Phonons: The Theory of Transport Phenomena in Solids* (*Oxford Classic Texts in the Physical Sciences*), 490–495 (Oxford University Press, England, 2001).
34. van Gorkom, R. P., Caro, J., Klapwijk, T. M. & Radelaar, S. Temperature and angular dependence of the anisotropic magnetoresistance in epitaxial Fe films. *Phys. Rev. B* **63**, 134432 (2001).
35. Ramos, R., Arora, S. K. & Shvets, I. V. Anomalous anisotropic magnetoresistance in epitaxial $Fe_3O_4$ thin films on MgO(001). *Phys. Rev. B* **78**, 214402 (2008).
36. Hikami, S., Larkin, A. I. & Nagaoka, Y. Spin-orbit interaction and Magnetoresistance in the two dimensional random system. *Prog. Theor. Phys.* **63**, 707–710 (1980).
37. Kim, H.-J. et al. Dirac versus Weyl fermions in topological insulators: Adler-Bell-Jackiw anomaly in transport phenomena. *Phys. Rev. Lett.* **111**, 246603 (2013).
38. Li, Q. et al. Chiral magnetic effect in $ZrTe_5$. *Nat. Phys.* **12**, 550 (2016).
39. Xiong, J., et al. P. Signature of the chiral anomaly in a Dirac semimetal–a current plume steered by a magnetic field. arXiv.1503.08179 (2015).
40. Zhao, Y. et al. Anisotropic fermi surface and quantum limit transport in high mobility three-dimensional dirac semimetal $Cd_3As_2$. *Phys. Rev. X* **5**, 031037 (2015).
41. Chen, Y. et al. Observation of Shubnikov-de Haas oscillations in large-scale Weyl semimetal $WTe_2$ films. *Chin. Phys. Lett.* **37**, 017104 (2020).
42. Xia, W. et al. The de Haas-van Alphen quantum oscillations in a three-dimensional Dirac semimetal $TiSb_2$. *Appl. Phys. Lett.* **116**, 142103 (2020).
43. Oveshnikov, L. N. et al. Superconductivity and Shubnikov - de Haas effect in polycrystalline $Cd_3As_2$ thin films. *Sci. Rep.* **10**, 4601 (2020).
44. Xiang, Z. J. et al. Angular-dependent phase factor of Shubnikov-de Haas oscillations in the Dirac semimetal $Cd_3As_2$. *Phys. Rev. Lett.* **115**, 226401 (2015).
45. Akiba, K. et al. Quantitative evaluation of Dirac physics in PbTe. *Phys. Rev. B* **98**, 115144 (2018).
46. Liu, Z. K. et al. Evolution of the Fermi surface of Weyl semimetals in the transition metal pnictide family. *Nat. Mater.* **15**, 27–31 (2016).
47. Shon, W. et al. Magnetic field-induced type II Weyl semimetallic state in geometrically frustrated Shastry-Sutherland lattice $GdB_4$. *Mater. Today Phys.* **11**, 100168 (2019).
48. Pariari, A., Dutta, P. & Mandal, P. Probing the Fermi surface of three-dimensional Dirac semimetal $Cd_3As_2$ through the de Haas–van Alphen technique. *Phys. Rev. B* **91**, 155139 (2015).
49. Zhang, C.-L. et al. Ultraquantum magnetoresistance in the Kramers-Weyl semimetal candidate $\beta-Ag_2Se$. *Phys. Rev. B* **96**, 165148 (2017).
50. Murakawa, H. et al. Detection of Berry's phase in a bulk Rashba semiconductor. *Science* **342**, 1490–1493 (2013).